Electrochimica Acta 537 (2025) 146843

Contents lists available at ScienceDirect

Electrochimica Acta

journal homepage: www.journals.elsevier.com/electrochimica-acta

MXene carbon nanofiber-coated V_2O_3 hollow nanospheres as a free-standing flexible anode for lithium-ion batteries

Binhe Feng [a], Deyang Zhang [a,*], Wenbo Guo [a], Di Wang [a], Jinbing Cheng [b], Kangwen Qiu [c], Mengzhen Du [a], Jin Chang [a,d], Paul K. Chu [e], Yongsong Luo [a,b,*]

[a] Henan Joint International Research Laboratory of New Energy Storage Technology, Xinyang Normal University, Xinyang 464000, PR China
[b] College of Physics and Electronic Engineering, Nanyang Normal University, Nanyang 473061, PR China
[c] College of Energy Engineering, Huanghuai University, Zhumadian, Henan 463000, China
[d] Pingdingshan University, Pingdingshan 467000, PR China
[e] Department of Physics, Department of Materials Science & Engineering, and Department of Biomedical Engineering, City University of Hong Kong, Tat Chee Avenue, Kowloon, Hong Kong, China

ARTICLE INFO

JEL:
71.35.-y
71.35.Lk
71.36.+c

Keywords:
V_2O_3
MXene
Electrospinning
Free-standing

ABSTRACT

V_2O_3 has emerged as a promising anode material for lithium-ion batteries (LIBs) owing to its high theoretical capacity (1073 mAh g^{-1}), abundant resources, and low toxicity. However, its practical application is severely hindered by rapid capacity decay caused by significant volume expansion during cycling and poor intrinsic electrical conductivity. Herein, we propose a novel strategy to construct a free-standing flexible electrode with a "0D@2D/1D" pearl-chain-like architecture (denoted as V_2O_3@MXene/CNFs) by integrating two-dimensional MXene ($Ti_3C_2T_x$) nanosheets with hollow V_2O_3 nanospheres via electrospinning. This design achieves triple synergistic effects to overcome existing limitations: 1) The MXene coating on hollow V_2O_3 nanospheres establishes efficient electron transport pathways while mitigating structural pulverization induced by volume changes; 2) The electrospinning process simultaneously suppresses restacking of MXene nanosheets and aggregation of V_2O_3 nanospheres, forming a three-dimensional interconnected conductive network; 3) The carbon nanofiber framework enhances mechanical robustness.The V_2O_3@MXene/CNFs anode delivers excellent electrochemical performance, including a capacity of 504.37 mAh g^{-1} at a current density of 0.1 A g^{-1} for 130 cycles and long cycle life (72.25 mAh g^{-1} at 5 A g^{-1} after 2000 cycles). The flexibility is assessed by assembling a pouch cell and folding it at various angles. The results reveal a new strategy to design flexible electrodes with a long cycling lifetime.

1. Introduction

Conventional V_2O_3/carbon nanofiber (CNF) electrodes exhibit promising flexibility but suffer from inherent limitations such as low electrical conductivity and severe volume expansion during cyclin [1,2]. To address these challenges, we propose a novel three-dimensional reticulated V_2O_3@MXene/CNF composite electrode by integrating MXene ($Ti_3C_2T_x$) [3,4]. The exceptional intrinsic conductivity and interlayer confinement effects of MXene synergistically reduce charge transfer resistance by 49 % (95.5 vs. 188 Ω) and mechanically buffer structural strai [5]. This performance significantly surpasses previously reported V_2O_3/CNF systems (<80 % retention). This strategy proposes a viable approach to advance flexible lithium-ion batteries with high energy density, improved cycling stability, and mechanical robustness.

Among the various electrode materials, transition metal oxides (TMOs) are highly competitive candidates because of their theoretical capacity [6,7]. In particular, vanadium trioxide (V_2O_3), which possesses a distinctive three-dimensional V-V framework, has a tunnel-like structure that facilitates Li^+ intercalation and unrestricted transfer of V 3d electrons. Furthermore, each V_2O_3 unit can accommodate up to six lithium ions by a conversion reaction, consequently yielding a theoretical capacity of 1073 mAh g^{-1} [8,9]. Nevertheless, V_2O_3 has some limitations as electrode materials. For instance, the sluggish electron/Li+ transport results in suboptimal rates and cycle life, thereby impeding the practical application of V_2O_3 [10].

MXene constitutes a novel class of two-dimensional transition metal

* Corresponding authors.
E-mail addresses: zdy@xynu.edu.cn (D. Zhang), ysluo@xynu.edu.cn (Y. Luo).

https://doi.org/10.1016/j.electacta.2025.146843
Received 6 April 2025; Received in revised form 2 July 2025; Accepted 3 July 2025
Available online 5 July 2025

carbide and nitride, it has high electrical conductivity, diverse surface functional groups, and good dispersion properties in a wide range of solvents [11,12]. Nevertheless, similar to other 2D materials, MXene nanosheets tend to aggregate due to van der Waals forces, thus reducing available active sites and reaction kinetics [13]. Gogotsi et al. have converted 2D MXene sheets into 1D nanofibers by electrospinning, which not only prevents the self-restacking of MXene but also enhances the electrical conductivity of the nanofibers [14].

Herein, MXene and V_2O_3 are combined to form a freestanding 3D reticulated composite consisting of 2D $Ti_3C_2T_x$-encapsulated hollow V_2O_3 nanospheres via electrospinning and annealing. The 0D@2D/1D nanochain (designated as V_2O_3@MXene/CNFs) is used to form a flexible electrode for high-performance LIBs [15]. In this configuration, the $Ti_3C_2T_x$ MXene coating enhances interfacial electron transport at nanosphere/carbon fiber interfaces via multifunctional mechanisms, Its high-conductivity 2D lamellae form 3D conductive networks, bridging gaps to reduce contact resistance. Surface -O/-OH/-F groups establish covalent Ti-O-C bonds and hydrogen-bonding networks, suppressing electron scattering while promoting charge transfer. Mechanical interlocking prevents nanosphere agglomeration, reinforced by $Ti_3C_2T_x$ MXene's inherent robustness. This integrated approach synergistically improves interfacial conductivity, charge kinetics, and environmental stability, while the nanochain mitigates volume expansion of V_2O_3 and facilitates the formation of a more stable solid electrolyte interphase (SEI) film to improve the cycling stability. As an anode in LIBs, V_2O_3@MXene/CNFs has many advantages, such the superior rate performance, stable long-term cycling stability, lightweight, as well as high energy density, in addition to not requiring binders and conductive additives [16]. It is incorporated into a pouch cell which functions normally in spite of folding at angles from 0° to 180°, thus boding well for commercial wearable electronic devices.

2. Experimental section

2.1. Fabrication of the V-P nanospheres

V-gly was synthesized by a hydrothermal method in which 0.7 mmol NH_4VO_3 was dispersed in a mixture of isopropyl alcohol and glycerol (25 mL) with a volume ratio of 5:1. The mixture was then transferred to a Teflon-lined autoclave and heated to 180 °C for six hours. The hydrothermal solution was then centrifuged repeatedly and freeze-dried to obtain the V-gly precursor. The V-P nanospheres were prepared by calcining V-gly at 350° for 1 h under argon at a heating rate of 1° min.

2.2. Synthesis of $Ti_3C_2T_x$ MXene

In order to etch Al from Ti_3AlC_2 precisely, 1 g LiF was added to 30 ml of HCl at a concentration of 9 mol/L, and then 40 % HF (5 ml) was added and stirred. 1 g of Ti_3AlC_2 powder was added slowly to the etching solution and stirred at 35 °C for 12 h and maintained at 35 °C under agitation for 12 h. The multilayered $Ti_3C_2T_x$ MXene was washed repeatedly with deionized water and centrifuged at 5000 rpm until the pH exceeded 6. The $Ti_3C_2T_x$ MXene solution was transferred to a bottle and shaken manually for one hour, after which it was sonicated in an Ar atmosphere for one more hour. The solution was washed repeatedly with deionized water and centrifuged at 4000 rpm to form the product. In order to use the product for electrospinning, the solvent (deionized water) was replaced with dimethylformamide (DMF) by repeated centrifugation (five times) at 10,000 rpm. A DMF solution containing $Ti_3C_2T_x$ MXene with a concentration of approximately 40 mg mL^{-1} was produced.

2.3. Synthesis of V_2O_3@MXene/CNFs

V_2O_3@MXene/CNF was synthesized by electrostatic spinning. 1 g of the V-P powder was dispersed in 5 ml of $Ti_3C_2T_x$ MXene, and PAN (0.6 g) was added and stirred overnight. The electrospinning solution was loaded into a 5 mL plastic syringe fitted with an 18 G blunt tip needle. A positive voltage (20 kV) was applied to the tip of the needle which was placed 12 cm from the collector. The solution was injected at a controlled rate of 0.4 mL/hour. The sample was electrospun in a relative humidity of less than 30 %. It was first pre-oxidized in air at 250 °C for 2 h at a rate of 2 °C min^{-1} and then carbonized in argon at 800 °C for 2 h at a rate of 2 °C min^{-1}. The prepared film was cut by a hand-held puncher and cut into a circular sheet with a diameter of 11 mm. The mass of the active material is about 0.003 g-0.004 g.

2.4. Synthesis of MXene/CNFs and V_2O_3/CNFs

For comparison, MXene/CNFs and V_2O_3/CNFs were prepared. V_2O_3/CNFs were fabricated in the same way as V_2O_3@MXene/CNFs but without the addition of $Ti_3C_2T_x$ MXene. Similarly, $Ti_3C_2T_x$ MXene underwent electrostatic spinning, followed by pre-oxidation and carbonization, to produce MXene/CNFs without the addition of V-P. The prepared film was cut by a hand-held puncher and cut into a circular sheet with a diameter of 11 mm. The mass of the active substance of V_2O_3/CNFs was about 0.002 *g*-0.003 g, and the mass of the active substance of MXene/CNFs was about 0.001 *g*

3. Results and discussion

NH_4VO_3 (ammonium vanadate), $C_3H_8O_3$ (propanetriol), and C_3H_8O (isopropanol) were used to prepare the V-gly pellets (Fig. S1) hydrothermally (Supporting Information) [17]. The precursor V-P (Fig. S2) was produced by heating under argon in a tube furnace. V-P is combined with $Ti_3C_2T_x$ MXene, after which polyacrylonitrile (PAN) is added and mixed [18]. The mixture underwent electrostatic spinning to form V_2O_3@MXene/CNFs nanofibers [19]. The nanofibers are pre-oxidized and carbonized to produce the V_2O_3@MXene/CNFs carbon nanofibers (Fig. 1).

The materials are characterized by scanning electron microscopy (SEM), and the contact angles on V_2O_3@MXene/CNFs were compared to those on V_2O_3/CNFs and MXene/CNFs. The Ti_3AlC_2 powder has a layered structure with a nearly undetectable spacing (Fig. S3). In contrast, the $Ti_3C_2T_x$, which undergoes etching with LiF/HCl MXene, displays a disordered lamellar configuration (Fig.S4) [20], suggesting that Al in the lamellae has been stripped during etching of the Ti_3AlC_2 powder. Fig. 2 (a1-a2) shows that MXene/CNFs form a discrete fiber-like structure after electrostatic spinning. The $Ti_3C_2T_x$ MXene nanosheets cover the carbon fibers uniformly without showing discernible agglomeration. Fig. 2 (b1-b2) shows V_2O_3@CNFs without adding $Ti_3C_2T_x$ MXene, and the V-P nanorods are also electrostatic spun to form the nanofibers. Fig. 2 (c1-c2) shows the formation of V_2O_3@MXene/CNFs after the addition of $Ti_3C_2T_x$ MXene. The $Ti_3C_2T_x$ MXene nanosheets attach firmly to the V-P nanoballs, which are wrapped in a pearl-like configuration and distributed uniformly on the carbon nanofibers. The hydrophilicity of the materials is verified by measuring the surface contact angle. As shown in Figure (a3-c3), the contact angles on V_2O_3@MXene/CNFs and V_2O_3/CNFs are 17.1° and 22.42°, respectively, indicating good hydrophilicity [21].

The nanostructure of V_2O_3@MXene/CNFs is probed by transmission electron microscopy (TEM) and energy-dispersive X-ray spectroscopy (EDS). As shown in Fig. 3a and d, the V_2O_3 nanospheres are wrapped in the carbon nanofibers like a chain of pearls. Fig. 3b and e provide clear evidence that the V_2O_3 nanospheres are hollow, with the single-layer MXene nanosheets attached firmly to the V_2O_3 nanospheres, giving rise to electronic pathways and mitigating volume expansion of the V_2O_3 nanospheres during charging and discharging [22]. Fig. 3c depicts the high-resolution transmission electron microscopy (HR-TEM) image of V_2O_3@MXene/CNF, revealing a lattice spacing of 0.2435 nm associated with the (110) plane of V_2O_3 in agreement with XRD [23]. Fig. 3f shows that the lattice spacing of 0.256 nm corresponds to the d-spacing of the

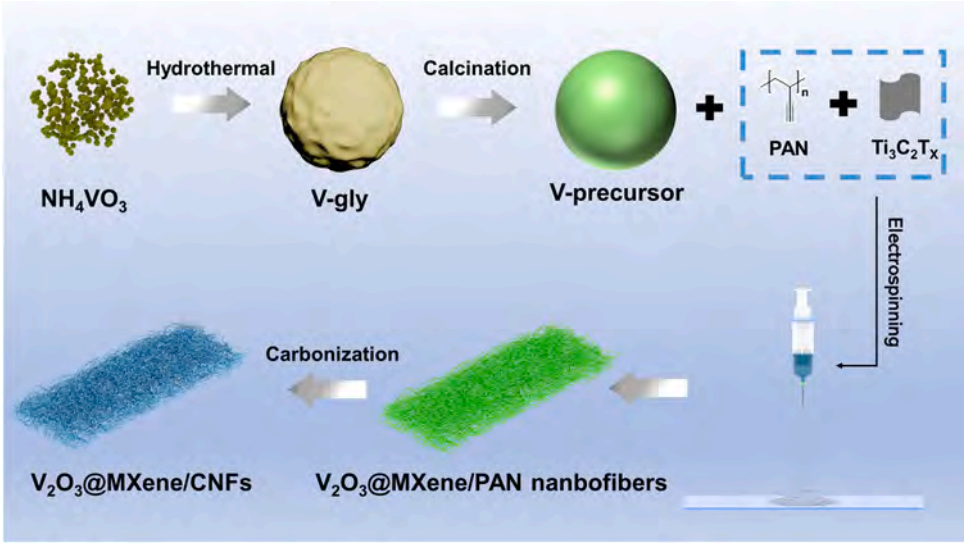

Fig. 1. Schematic showing the preparation of V_2O_3@MXene/CNFs carbon nanofibers.

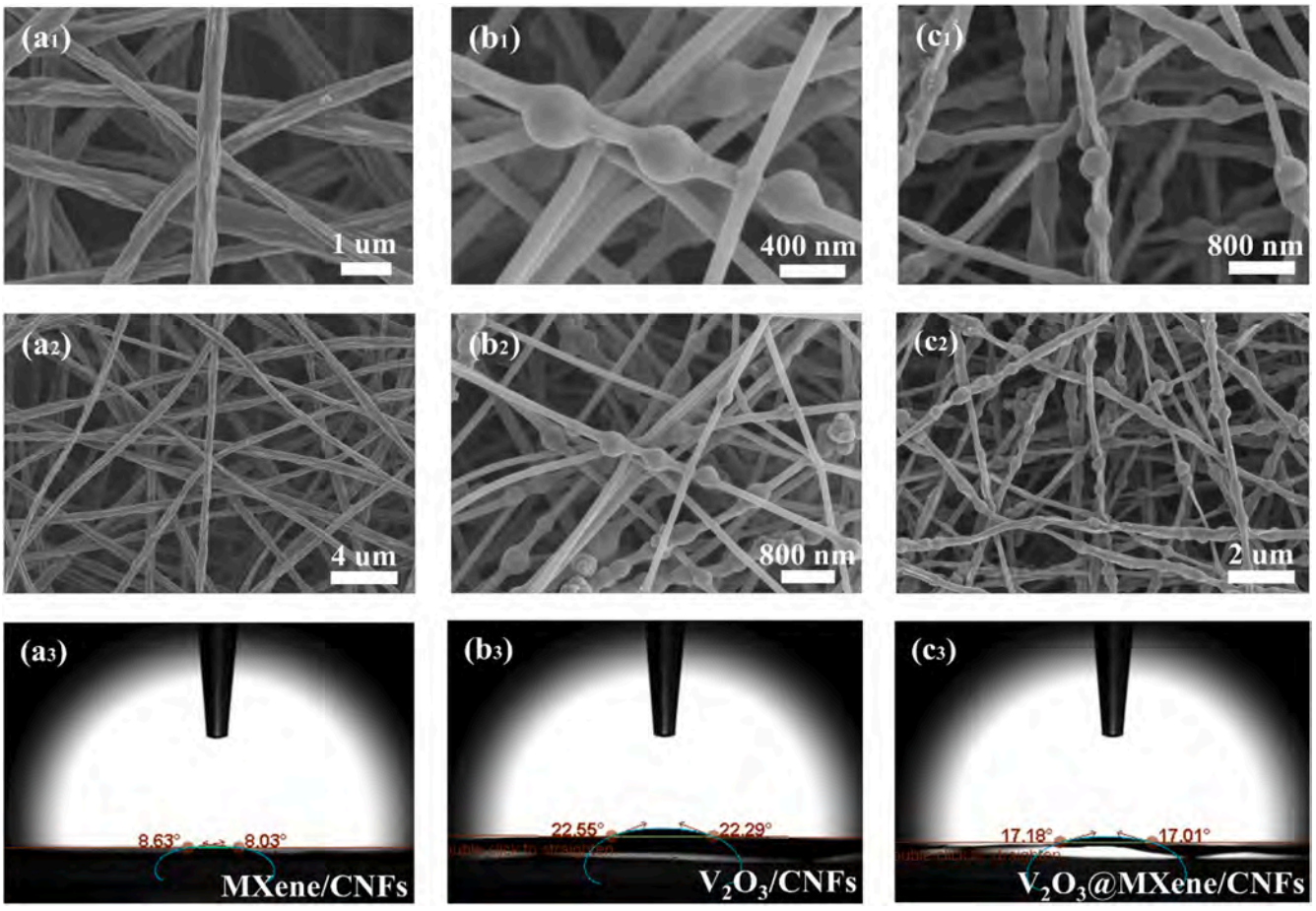

Fig. 2. (a1-a2) SEM images of MXene/CNFs; (b1-b2) SEM images of V_2O_3/CNFs; (c1-c2) SEM images of V_2O_3@MXene/CNFs; (a3-c3) Images showing the surface contact angles on MXene/CNFs, V_2O_3/CNFs, and V_2O_3@MXene/CNFs.

(100) plane of $Ti_3C_2T_x$ [24]. The distributions C, N, Ti, V, and O are shown in elemental maps (Fig. 3g-i).

The structure and composition of V_2O_3@MXene/CNFs are analyzed by X-ray diffraction (XRD), X-ray photoelectron spectroscopy (XPS), and Raman scattering. Fig. 4a shows the XRD patterns of V_2O_3@MXene/CNFs, V_2O_3/CNFs, and MXene/CNFs, revealing the rhombohedral crystalline phase (JCPDS 34–0187) and confirming the successful preparation of V_2O_3@MXene/CNFs [25]. The Raman spectra of V_2O_3@MXene/CNFs and V_2O_3/CNFs in Fig. 4b show peaks from V_2O_3 at 138.803, 276.331, 685.03, and 988.301 cm^{-1} and the disordered-induced d-band of V_2O_3@MXene/CNFs at 1350.01 cm^{-1}. The G-band of graphite at 1590.98 cm^{-1} shows a larger D band to G

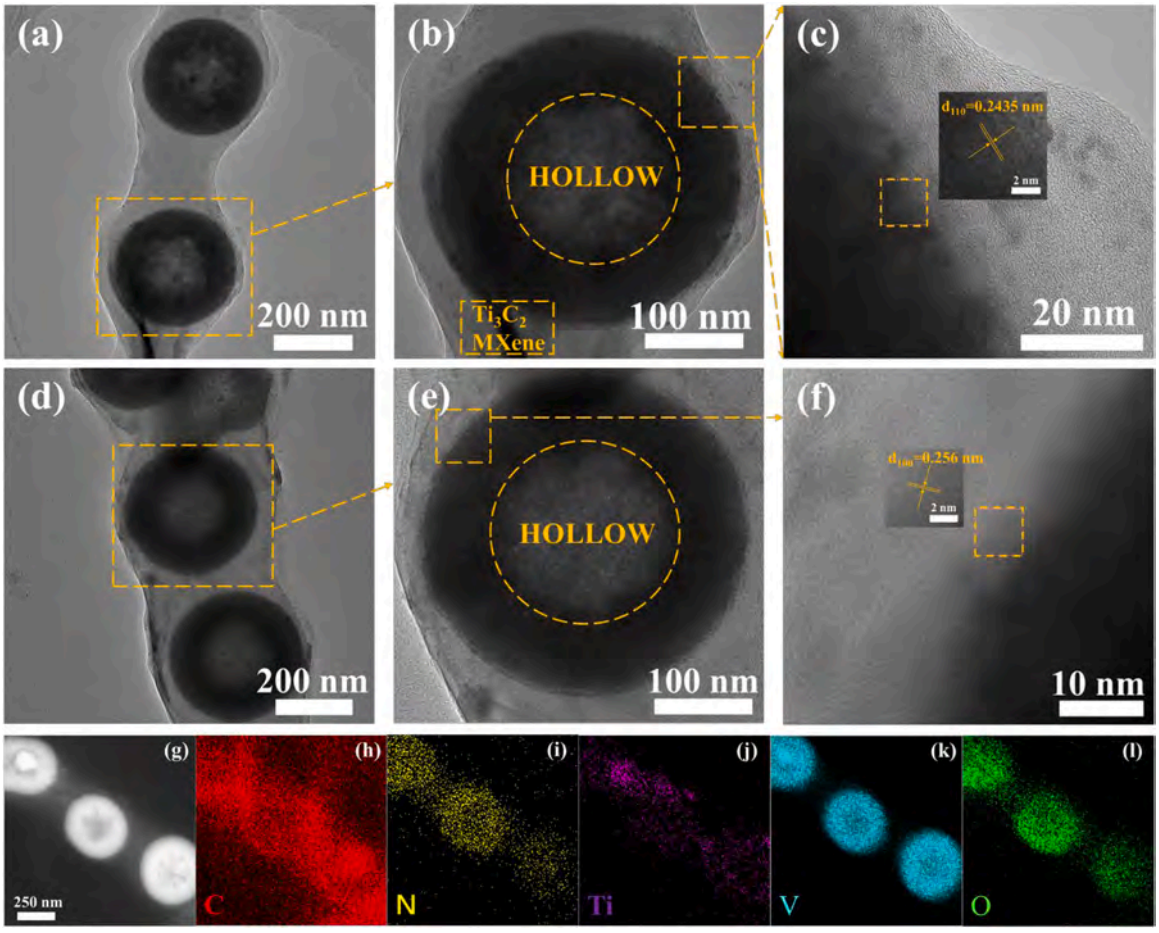

Fig. 3. (a, b, d, e) TEM images of V_2O_3@MXene/CNFs; (c, f) HR-TEM images of V_2O_3@MXene/CNFs; (g, h, i, j, k, l) EDS elemental maps of V_2O_3@MXEene/CNFs.

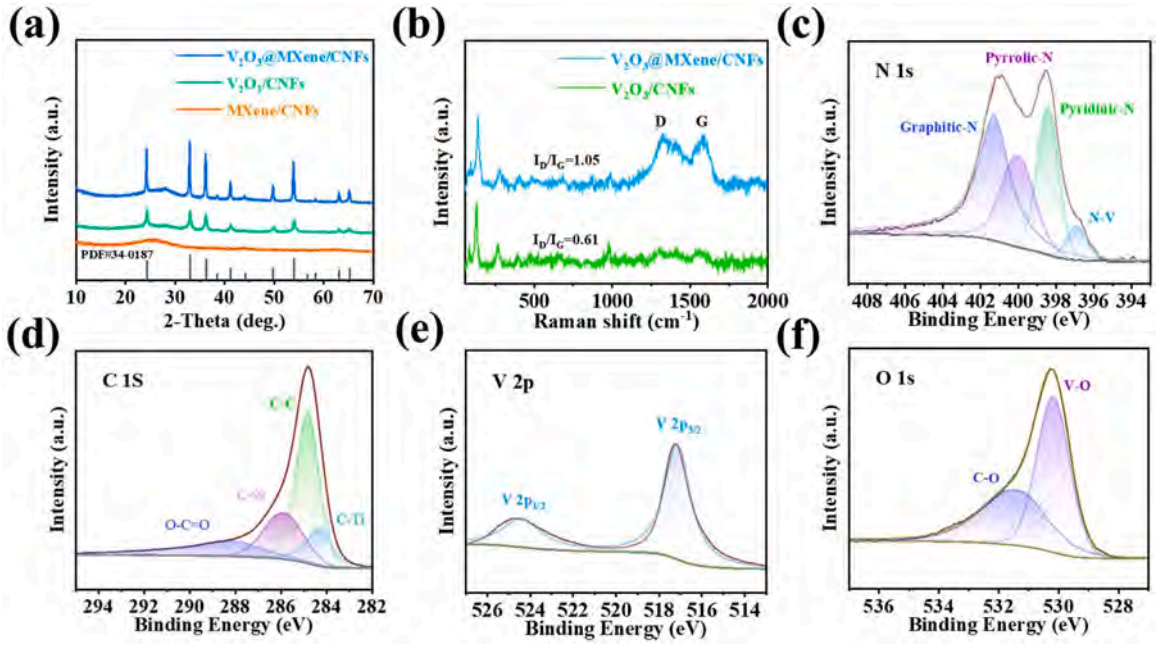

Fig. 4. (a) XRD patterns of V_2O_3@MXene/CNFs, V_2O_3/CNFs, and MXene/CNFs; (b) Raman scattering spectra of V_2O_3@MXene/CNFs and V_2O_3/CNFs; (c-f) XPS spectra of V_2O_3@MXene/CNFs: (c) N 1 s, (d) C 1S, (e) V 2p, and (f) O 1 s.

band ratio (1.05) of V_2O_3@MXene/CNFs compared to 0.61 of V_2O_3/CNFs, implying enhanced sp2 domains of carbon, defects, and disorders. The three peaks of MXene/CNFs at 266.611, 419.126, and 601.331 corroborate successful synthesis (Fig. S5) [26,27]. Fig. 4d shows peaks at 283.74 (eV), 285.89 (eV), 287.93 (eV), and 284.25 (eV) corresponding to C—C, $C=N$, O—$C=O$, and C-Ti, respectively [24,28], and Fig. 4c reveals graphitic N (401.28 eV), pyrrole N (400.08 eV), pyridine N (398.38 eV), and N-V (396.88 eV) [29]. Fig. S6 shows peaks at 457.78 eV,458.68 eV for Ti-C, Ti^{4+},respectively [30,31], while Fig. 4e shows peaks at 517.18 eV and 524.38 eV for V $2p^{3/2}$ and V $2p^{1/2}$, respectively, indicative of V^{3+}, confirming the formation of V_2O_3 [7,23]. Fig. 4f shows two peaks at 530.18 and 531.48 for V-O and C—O, respectively [23,32], indicating that V_2O_3 has strong interactions with the carbon nanofibers [26,33]. The specific surface area and pore size distribution of V_2O_3@MXene/CNFs were characterized via N_2 adsorption-desorption isotherms. As illustrated in Figure S8, the isotherm exhibits a distinct Type IV curve, confirming the presence of mesoporous structures. The Brunauer-Emmett-Teller (BET) specific surface area was calculated to be 14.9526 $cm^2\ g^{-1}$, while the Barrett-Joyner-Halenda (BJH) pore size distribution (Fig. S9) reveals that the majority of pores are concentrated within 2–40 nm, consistent with the isothermal analysis. These mesopores primarily originate from the pyrolysis of carbon fibers during pre-oxidation and carbonization processes, where volatile byproducts (e.g., CO_2, HCN, and NH_3) are released, generating interconnected pore networks. The hierarchically porous architecture, coupled with the high specific surface area, facilitates efficient electrolyte infiltration, shortens Li^+ diffusion pathways, and alleviates volumetric strain during cycling, thereby synergistically enhancing the electrochemical performance, as evidenced by the superior rate capability and cycling stability [34].

In order to determine the electrochemical properties of V_2O_3@MXene/CNFs, V_2O_3/CNFs, and MXene/CNFs, they are incorporated into lithium-ion batteries as anodes. Fig. 5a shows the cyclic voltammograms of the first three cycles of V_2O_3@MXene/CNFs at a scanning rate of 0.1 mV s^{-1} in the voltage range of 0.01–3 V. There is a significant reduction peak at 0.84 V in the first cathode scan but it disappears two cycles later due to the formation of a solid electrolyte interface(SEI) [23,35]. In the anode section, a wide anode peak appears at 0.75 V to 2 V from the de-impingement of lithium ions. The curves almost overlap in subsequent cycles, indicating that V_2O_3@MXene/CNFs have good electrochemical reversibility [24,26]. The MXene coating ($Ti_3C_2T_x$) suppresses V_2O_3 volume expansion and stabilizes the solid electrolyte interphase (SEI) through synergistic integration of conductive nanosheet-enabled homogeneous electron/Li^+ transport, interfacial adhesion reinforced by covalent Ti–O–C bonds and hydrogen bonding, and hydrophilicity-driven electrolyte infiltration to mitigate polarization and parasitic reactions [36]. Fig. 5b shows that V_2O_3@MXene/CNFs have the highest specific capacity and the optimal rates. The discharge capacities of V_2O_3@MXene/CNFs are 651.88, 563.66, 485.67, 386.56, 300.62, and 118.02 mAh g^{-1} at current densities of 0.1, 0.2, 0.5, 1, 2, and 5 A g^{-1}, respectively. The capacities of V_2O_3/CNFs and MXene/CNFs at current densities of 0.1, 0.2, 0.5, 1,2 and 5 A g^{-1} are 526.92, 412.44, 365.13, 313.50, 190.78, 84.73 mAh g^{-1} and 427.78, 329.88, 263.33, 207.76, 170.95, 93.06 mAh g^{-1}, respectively. It can be seen from the data that the capacity of V_2O_3/CNFs and MXene/CNFs is lower than that of V_2O_3@MXene/CNFs. After cycling for 10 revolutions at each current density, the capacity returns to 596.54 when the current density returns to 0.1 A g^{-1} again. Good stability is

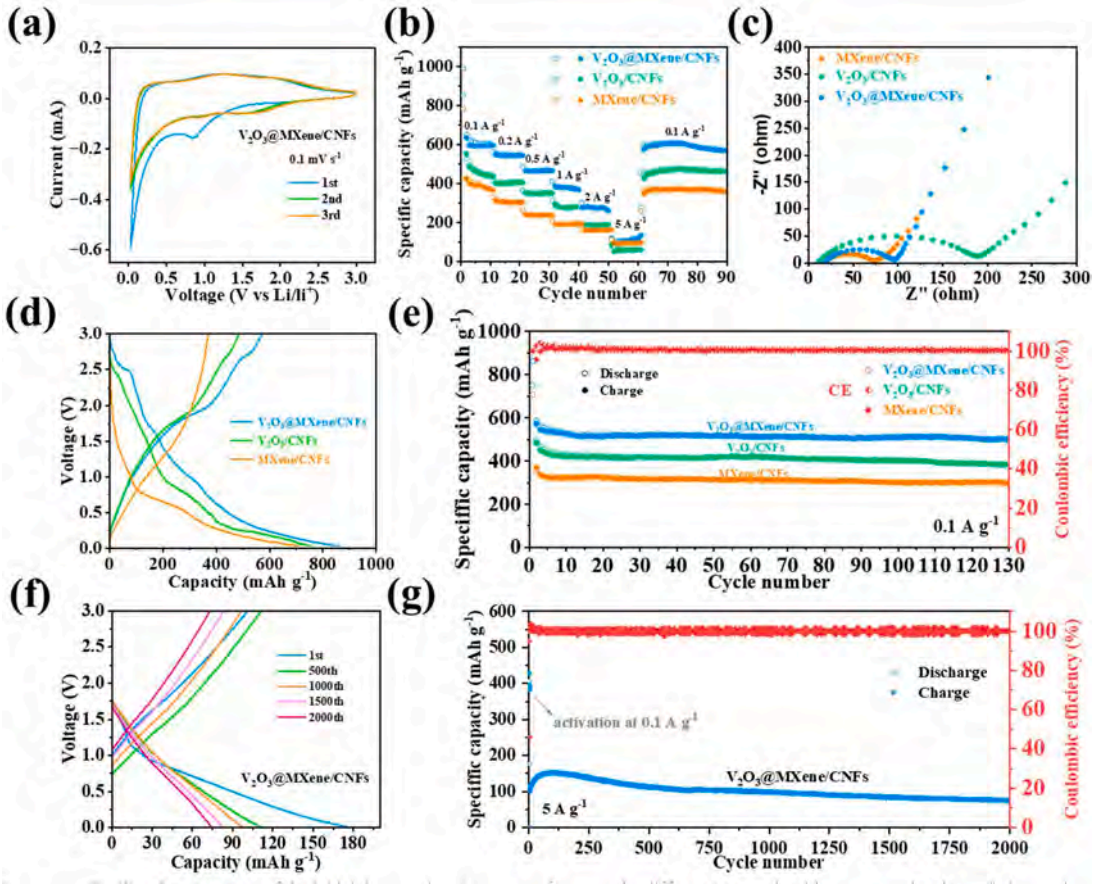

Fig. 5. (a) Cyclic voltammograms of the initial three cycles; (b) Rate performance for different current densities; (c) Nyquist plots; (d) Comparison of the first galvanostatic charging/discharging curves at 0.1 A g^{-1}; (e) Cycling properties of V_2O_3@MXene/CNF, V_2O_3/CNF, and MXene/CNF at a current density of 0.1 A g^{-1}; (f) V_2O_3@MXene/CNFs for various cycles at a current density of 5 A g^{-1}; (g) Cycling properties of V_2O_3@MXene/CNFs at a large current density of 5 A g^{-1}.

shown for 30 cycles. Fig. 5c and S11 shows the Nyquist plots and fitting result of the MXene/CNFs, V_2O_3/CNFs, and V_2O_3@MXene/CNFs electrodes . The semicircle in the figure corresponds to the charge transfer resistance in the medium-high frequency region (Rct), and the slashes in the lower frequency region correspond to Warburg impedance. The higher the slope of the Warburg line, the better the ionic conductivity of the electrode [24,37]. The Rct values of V_2O_3@MXene/CNFs, V_2O_3/CNFs, and MXene/CNFs electrodes are 95.5 Ω, 188 Ω, and 71.8 Ω, respectively. Hence, the incorporation of Ti_3C_2 reduces the charge transfer impedance of V_2O_3@MXene/CNFs [18,24]. Furthermore, four-probe measurements revealed that the MXene-doped composite of V_2O_3@MXene/CNFs exhibits significantly enhanced electrical conductivity compared to the conventional V_2O_3/carbon fiber architecture (Supplementry Table 2). Fig. 5D presents the first galvanostatic charging/discharging curves of V_2O_3@MXene/CNFs, V_2O_3/CNFs, and MXene/CNFs at a rate of 0.1 A g^{-1}. The first discharge capacities and Coulombic efficiencies (CE) of the three materials are 862.22/66 %, 750.94/64 %, and 708.38/52 % (IC), respectively. The low ICE can be attributed to the formation of the solid electrolyte interphase (SEI) and electrolyte decomposition [23,38]. Fig. 5e illustrates the cycling characteristics of V_2O_3@MXene/CNFs, V_2O_3/CNFs, and MXene/CNFs at a current density of 0.1 A g^{-1} for 130 cycles. The V_2O_3@MXene/CNFs electrode exhibits superior capacity retention and cyclic stability compared to the other two materials. Fig. 5g shows the cycling characteristics of V_2O_3@MXene/CNFs at high current densities, and V_2O_3@MXene/CNFs retain nearly the same capacity even at a current density of 5 A g^{-1}, while the structure does not change after 2000 cycles (Fig. 5f).

To investigate the Li^+ storage capacity of V_2O_3@MXene/CNFs, cyclic voltammetry (CV) is carried out at various scan rates from 0.2 to 1 mV s^{-1} (Fig. 6a). The storage capacity of Li^+ can be determined by the following equation:

$$i = av^b$$

where i is the peak current, v is the scanning rate, and a and b are arbitrary values [26,39]. When b approaches 1, the capacitive behavior is predominant, whereas when b is near 0.5, diffusion control is more significant. As shown in Fig. 6b, the b value of the cathodic peak is 0.93, while that of the anodic peak is 0.82, suggesting that capacitive behavior dominates. The contributions of capacitance and diffusion can be quantified by the equation [26,40]:

$$i = k_1 v + k_2 v^{\frac{1}{2}}$$

where $k_1 v$ represents the contribution from capacitance and $k_2 v^{\frac{1}{2}}$ is the contribution from diffusion. To quantify the contribution of capacitance to the total capacity, the values of k_1 are derived at various scanning rates by the aforementioned formula. The pseudocapacitance contribution of V_2O_3@MXene/CNFs increases with scanning rates (Fig. S7), reaching 82 % at a scanning rate of 2 mV s^{-1} (Fig. 6c). The significant pseudocapacitance contribution of V_2O_3@MXene/CNFs accounts for its excellent rate performance.

To further investigate the Li^+ reaction kinetics of V_2O_3@MXene/CNFs, constant current intermittent titration (GITT) is employed (Fig. 6d) at a current density of 0.1 A g^{-1} and with each pulse lasting 10 min and a relaxation period of 10 min. According to Fick's second law:

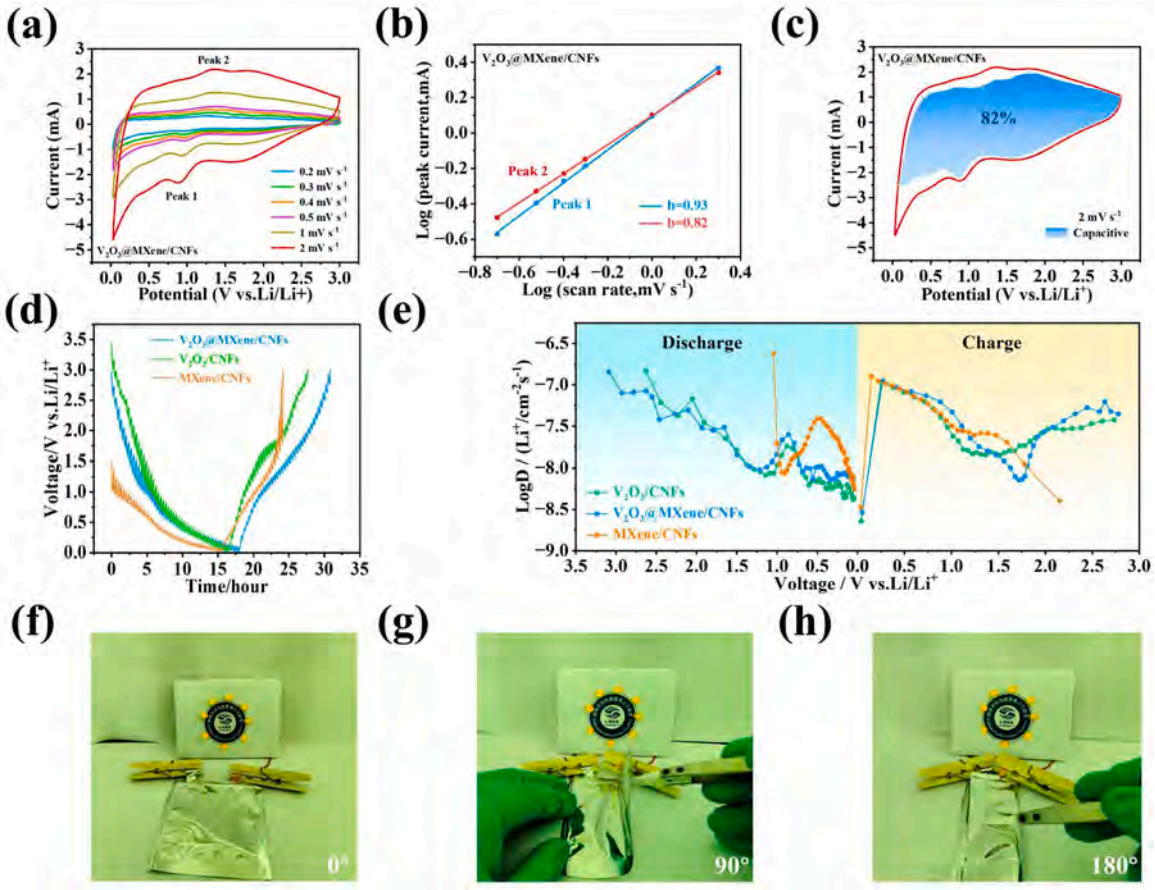

Fig. 6. (a) CV profiles of V_2O_3@MXene/CNFs at different scanning rates; (b) Relationship between peak currents and scanning rates; (c) Capacitive contribution (shaded area) at 2 mV s^{-1}; (d) GITT curves; (e) Lithium-ion diffusion coefficients of V_2O_3@MXene/CNFs, V_2O_3/CNFs, and MXene/CNFs at different charging and discharging voltages. (f-h) Qualitative assessment of the insensitivity to folding of the pouch cell.

$$D = \frac{4}{\pi\tau}\left(\frac{n_m V_m}{S}\right)^2\left(\frac{\Delta E_S}{\Delta E_\tau}\right)^2.$$

the Li^+ diffusion coefficient can be calculated [41,42]. Here, τ represents the current pulse time, n_m and V_m denote the molar mass and molar volume of the active materials, respectively, and ΔE_S and ΔE_τ are the potential differences at the steady state and during the current pulse, respectively [43]. As shown in Fig. 6e, during discharging, the diffusion coefficients D of V_2O_3@MXene/CNFs, V_2O_3/CNFs, and MXene/CNFs are 1.44×10^{-7}–2.92×10^{-9} $cm^2\ s^{-1}$, 1.48×10^{-7}–2.27×10^{-9} $cm^2\ s^{-1}$, and 2.41×10^{-7}–3.37×10^{-9} $cm^2\ s^{-1}$, respectively. During charging, they are 1.21×10^{-7}–4.45×10^{-8} $cm^2\ s^{-1}$,1.1×10^{-7}–3.77×10^{-8} $cm^2\ s^{-1}$, and 1.27×10^{-7}–4×10^{-9} $cm^2\ s^{-1}$ respectively, demonstrating improved electrochemical kinetics.

To evaluate the application potential of V_2O_3@MXene/CNFs, a flexible pouch cell is assembly. When the pouch cell is connected to the negative electrode, the LED lights up (Fig. 6f). During folding at a 90° angle, the intensity of the LED light remains unchanged (Fig. 6 g), Even if the pouch cell is folded to 180°, there is still no change in the brightness of the LED (Fig. 6h), even under a stable cycling condition at a high current density of 5 A g^{-1} combined with a bending angle of 180°, the electrode retains a capacity of 63.922 mAh g^{-1} after 800 cycles. To further evaluate the structural and chemical stability of the composite, comprehensive post-cycling characterizations were performed on the V_2O_3@MXene/CNFs electrode after 800 cycles. XPS analysis revealed a slight upward shift in the binding energies of V $2p^{3/2}$ and V $2p^{1/2}$, transitioning from 517.18 eV and 524.38 eV (pristine state) to 517.98 eV and 525.28 eV, respectively(Fig. S 14). This binding energy evolution likely originates from partial oxidation of vanadium species (e.g., $V^{3+} \rightarrow V^{4+}$) during prolonged lithium-ion intercalation/deintercalation processes. Crucially, SEM and TEM observations (Fig. S 15 and S16) demonstrated negligible morphological deformation or structural collapse of the V_2O_3 hollow nanospheres, while the MXene-carbon nanofiber network retained its integrated conductive framework. The preservation of both nanoscale architecture and interfacial bonding under extreme deformation conditions unequivocally confirms the exceptional mechanical-electrochemical stability of the composite, which synergistically contributes to its long-term cycling robustness. The material of V_2O_3@MXene/CNFs demonstrating exceptional mechanical-electrochemical stability under extreme deformation, corroborating the outstanding flexibility, mechanical strength, and commercial potential.

4. Conclusion

The integration of MXene ($Ti_3C_2T_x$) into the V_2O_3/carbon nanofiber (CNF) architecture introduces multifunctional enhancements that transcend the limitations of conventional V_2O_3/CNF electrodes. First, the MXene coating establishes a highly conductive network, reducing the charge transfer resistance (Rct) by 49.2 % (from 188 Ω to 95.5 Ω), which significantly accelerates the reaction kinetics. Second, the MXene-encapsulated hollow V_2O_3 nanospheres form a mechanically robust "pearl-chain" structure, effectively buffering volume expansion and achieving 82.3 % capacity retention after 2000 cycles at 5 A g^{-1}, a 64.6 % improvement over prior V_2O_3/CNF systems. Third, the hierarchical design optimizes lithium-ion diffusion,while the hydrophilic MXene surface facilitates uniform electrolyte infiltration. By assembling a pouch cell and folding it at various angles, the V_2O_3@MXene/CNFs electrode shows excellent flexibility. The results reveal a novel strategy to design flexible and self-supporting electrode materials with high energy densities, superior rate performance, and outstanding cyclic stability.

CRediT authorship contribution statement

Binhe Feng: Writing – original draft, Data curation. **Deyang Zhang:** Funding acquisition. **Wenbo Guo:** Data curation. **Di Wang:** Supervision. **Jinbing Cheng:** Resources. **Kangwen Qiu:** Funding acquisition. **Mengzhen Du:** Data curation. **Jin Chang:** Formal analysis. **Paul K. Chu:** Validation. **Yongsong Luo:** Supervision.

Declaration of competing interest

The authors declare that they have no known competing financial interests or personal relationships that could have appeared to influence the work reported in this paper. This research was conducted in the absence of any commercial or financial relationships that could be construed as a potential conflict of interest. All funding sources for this study are acknowledged in the manuscript, and no external entities influenced the design, execution, analysis, or interpretation of the research findings.

Acknowledgements

This work was financially supported by the National Natural Science Foundation of China (No. 52272219, No. 52401236), Nanhu Scholars Program for Young Scholars of XYNU, Graduate Research and Innovation Fund of XYNU (2024KYJJ006), Natural Science Foundation of Henan province (No. 242300420348) and City University of Hong Kong Donation Research Grants (9220061 and DON-RMG 9229021).

Supplementary materials

Supplementary material associated with this article can be found, in the online version, at doi:10.1016/j.electacta.2025.146843.

Data availability

Data will be made available on request.

References

[1] P. Kokmat, P. Matsayamat, K. Wongrach, P. Surinlert, A. Ruammaitree, Improvement of specific capacity of lithium iron phosphate battery by increasing the surface area and electrical conductivity of cathode electrode using graphene foam, J. Metals, Mater. Miner. 33 (4) (2023) 1779, https://doi.org/10.55713/jmmm.v33i4.1779.

[2] Y.-H. Zhao, Z.-Q. Dai, C.-W. Yang, D. Xu, J. Zhao, S.-H. Chen, J. Yi, Y.-P. Lei, X.-Y. Zhang, J.-Q. Qin, Heterojunction structure of LiV_3O_8-LiV_6O_{15} cathode material with multiple electron reactions, Rare Met. 44 (4) (2025) 2815–2821, https://doi.org/10.1007/s12598-024-03121-w, 2815.

[3] B. Sun, M. Zhang, H. Yuan, W. Wei, Z. Lin, J. Chang, Y. Hao, A. Three-Dimensional, Flexible conductive network based on an MXene/rubber composite for lithium metal anodes, ACS Appl. Mater. Interfaces 17 (2) (2024) 3248–3256, https://doi.org/10.1021/acsami.4c15406, 3248.

[4] Z. Li, T.T. Beyene, K. Zhu, D. Cao, Realizing fast plating/stripping of high-performance Zn metal anode with a low Zn loading, J. Metals, Mater. Miner. 34 (2) (2024) 2009, https://doi.org/10.55713/jmmm.v34i2.2009.

[5] W. Liu, J. Cao, F. Song, D.-D. Zhang, M. Okhawilai, J. Yi, J.-Q. Qin, X.-Y. Zhang, A double transition metal $Ti_2NbC_2T_x$ MXene for enhanced lithium-ion storage, Rare Met. 42 (1) (2022) 100–110, https://doi.org/10.1007/s12598-022-02120-z, 100.

[6] D. McNulty, D.N. Buckley, C. O'Dwyer, V_2O_3 polycrystalline nanorod cathode materials for Li-ion batteries with long cycle life and high capacity retention, Chem. Elect. Chem. 4 (8) (2017) 2037–2044, https://doi.org/10.1002/celc.201700202, 2037.

[7] D. Zhang, G. Li, B. Li, J. Fan, X. Liu, D. Chen, L. Li, A facile strategy to fabricate V_2O_3/Porous N-doped carbon nanosheet framework as high-performance anode for lithium-ion batteries, J. Alloys Compd. 789 (2019) 288–294, https://doi.org/10.1016/j.jallcom.2019.02.251, 288.

[8] F. Liang, R. Zheng, Z. Zou, F. Long, S. Zhang, S. Zhong, S. Jia, J. Nong, Y. Wang, L. Song, Vanadium oxide-based battery materials, Ionics (Kiel) 30 (11) (2024) 6729–6755, https://doi.org/10.1007/s11581-024-05751-7, 6729.

[9] D. Zhao, C. Wang, Y. Ding, M. Ding, Y. Cao, Z. Chen, Will vanadium-based electrode materials become the future choice for metal-ion batteries? Chem. Sus. Chem. 15 (12) (2022) 202200479 https://doi.org/10.1002/cssc.202200479.

[10] P. Liu, K. Zhu, Y. Xu, K. Bian, J. Wang, G.a. Tai, Y. Gao, H. Luo, L. Lu, J. Liu, Hierarchical porous intercalation-type V_2O_3 as high-performance anode materials

for Li-ion batteries, Chem. – A Eur. J. 23 (31) (2017) 7538–7544, https://doi.org/10.1002/chem.201700369, 7538.
[11] Y. Chen, H. Yang, Z. Han, Z. Bo, J. Yan, K. Cen, K.K. Ostrikov, MXene-based electrodes for supercapacitor energy storage, Energy Fuels 36 (5) (2022) 2390–2406, https://doi.org/10.1021/acs.energyfuels.1c04104, 2390.
[12] W. Wang, M. Ma, Y. Song, Z. Wang, C. Bian, R. Cai, X. Wang, X. Zhu, Electrochemically intercalated Ti_3C_2 MXene bulk for expanding interlayer spacing and enhancing supercapacitor performance, Inorg. Chem. 63 (2024) 4320633–4320642, https://doi.org/10.1021/acs.inorgchem.4c03280.
[13] Y. Zhu, J. Ma, P. Das, S. Wang, Z.S. Wu, High-voltage MXene-based supercapacitors: present status and Future perspectives, Small Methods 7 (8) (2023) 2201609, https://doi.org/10.1002/smtd.202201609.
[14] Z. Ling, C.E. Ren, M.-Q. Zhao, J. Yang, J.M. Giammarco, J. Qiu, M.W. Barsoum, Y. Gogotsi, Flexible and conductive MXene films and nanocomposites with high capacitance, Proc. Natl Acad. Sci. 111 (47) (2014) 16676–16681, https://doi.org/10.1073/pnas.1414215111, 16676.
[15] I. Mjejri, A. Rougier, M. Gaudon, Low-cost and facile synthesis of the vanadium oxides V_2O_3, VO_2, and V_2O_5 and their magnetic, thermochromic and electrochromic properties, Inorg. Chem. 56 (2017) 31734–31741, https://doi.org/10.1021/acs.inorgchem.6b02880.
[16] D. Wang, H. Yan, Y. Yang, J. Cheng, Y. Lu, Y. Luo, H. Pang, Promoting polysulfide bidirectional conversion by one-dimensional p-n junctions for Li-S batteries, Sci. China Mater. 67 (1) (2023) 93–106, https://doi.org/10.1007/s40843-023-2666-1, 93.
[17] M. Zhao, Y. Lu, Y. Yang, M. Zhang, Z. Yue, N. Zhang, T. Peng, X. Liu, Y. Luo, A vanadium-based oxide-nitride heterostructure as a multifunctional sulfur host for advanced Li–S batteries, Nanoscale 13 (30) (2021) 13085–13094, https://doi.org/10.1039/d1nr03763c, 13085.
[18] Y. Guo, D. Zhang, Z. Bai, Y. Yang, Y. Wang, J. Cheng, P.K. Chu, Y. Luo, MXene nanofibers confining MnO_x nanoparticles: a flexible anode for high-speed lithium ion storage networks, Dalton Trans. 51 (4) (2022) 1423–1433, https://doi.org/10.1039/d1dt03718h, 1423.
[19] T. Peng, N. Zhang, Y. Yang, M. Zhang, R. Luo, C. Chen, Y. Lu, Y. Luo, Crystal facet engineering of MXene-derived TiN nanoflakes as efficient bidirectional electrocatalyst for advanced lithium-sulfur batteries, Small 18 (2022) 382202917, https://doi.org/10.1002/smll.202202917.
[20] C.E. Shuck, MXenes are materials, not chemicals: synthesis factors that influence MXene properties, MRS Commun 13 (6) (2023) 957–970, https://doi.org/10.1557/s43579-023-00442-2, 957.
[21] H. Zhou, F. Wang, Y. Wang, C. Li, C. Shi, Y. Liu, Z. Ling, Study on contact angles and surface energy of MXene films, RSC Adv. 11 (10) (2021) 5512–5520, https://doi.org/10.1039/d0ra09125a, 5512.
[22] J. Xu, Z. Dong, K.-J. Huang, T. Wang, Y. Qi, Y. Sun, X. Wu, Preparation of large layer spacing bimetallic sulfide hollow nanosphere for high-energy battery system application, Appl. Surf. Sci. 637 (2023) 157959, https://doi.org/10.1016/j.apsusc.2023.157959.
[23] T. Zhang, L. Zhang, L. Zhao, X. Huang, W. Li, T. Li, T. Shen, S. Sun, Y. Hou, Free-standing, foldable V_2O_3/multichannel carbon nanofibers electrode for flexible Li-ion batteries with Ultralong Lifespan, Small 16 (47) (2020) 2005302, https://doi.org/10.1002/smll.202005302.
[24] Y. Guo, D. Zhang, Y. Yang, Y. Wang, Z. Bai, P.K. Chu, Y. Luo, MXene-encapsulated hollow Fe_3O_4 nanochains embedded in N-doped carbon nanofibers with dual electronic pathways as flexible anodes for high-performance Li-ion batteries, Nanoscale 13 (8) (2021) 4624–4633, https://doi.org/10.1039/d0nr09228b, 4624.
[25] J. Sun, C. Lu, Q. Tian, Y. Mei, J. Peng, Y. Ding, V_2O_3/MoS_2 microspheres as a high-performance anode for Li-storage, Appl. Surf. Sci. 513 (2020) 145756, https://doi.org/10.1016/j.apsusc.2020.145756.
[26] Q. Lai, B. Yin, Y. Dou, Q. Zhang, Y. Zhu, Y. Yang, Electrospun carbon nanofiber-supported V_2O_3 with enriched oxygen vacancies as a free-standing high-rate anode for an all-vanadium-based full battery, Carbon Energy 6 (9) (2024) 517, https://doi.org/10.1002/cey2.517.
[27] Z. Wang, D. Zhang, Y. Guo, H. Jiang, D. Wang, J. Cheng, P.K. Chu, H. Yan, Y. Luo, $Ti_3C_2T_x$ MXene-embedded MnO_2-based hydrophilic electrospun carbon nanofibers as a freestanding electrode for supercapacitors, Chem. Commun. 59 (96) (2023) 14309–14312, https://doi.org/10.1039/d3cc03925k, 14309.
[28] Z. Li, Z. Long, H. Dai, Z. Yan, K. Liu, H. Qiao, K. Wang, W. Li, $Ti_3C_2T_x$ MXene@metal-organic frameworks-derived bead-like carbon nanofibers heterostructure aerogel for enhanced performance lithium/sodium storage, J. Power Sources 606 (2024) 234586, https://doi.org/10.1016/j.jpowsour.2024.234586.
[29] Z. Wu, Q. Chen, C. Li, L. Zhu, Y. Huang, X. Zhu, X. Zhu, Y. Sun, Hydrogel-derived nitrogen-doped porous carbon framework with vanadium nitride decoration for supercapacitors with superior cycling performance, J. Mater. Sci. Technol. 155 (2023) 167–174, https://doi.org/10.1016/j.jmst.2023.01.031, 167.
[30] J. Halim, K.M. Cook, M. Naguib, P. Eklund, Y. Gogotsi, J. Rosen, M.W. Barsoum, X-ray photoelectron spectroscopy of select multi-layered transition metal carbides (MXenes), Appl. Surf. Sci. 362 (2016) 406–417, https://doi.org/10.1016/j.apsusc.2015.11.089, 406.
[31] Y. Li, J. Zhang, Y. Cheng, K. Feng, J. Li, L. Yang, S. Yin, Stable $TiVCT_x$/poly-o-phenylenediamine composites with three-dimensional tremella-like architecture for supercapacitor and Li-ion battery applications, Chem. Eng. J. 433 (2022) 134578, https://doi.org/10.1016/j.cej.2022.134578.
[32] Y. Tian, J. Zhang, T.A. Otitoju, H. Wang, H. Chen, L. Zhu, Z. Feng, T. Sun, Effective transportation of electrons/Li ions in V_2O_3 nanoparticle/carbon-coated stainless steel composite electrodes for lithium-ion storage, J. Ind. Eng. Chem. 114 (2022) 297–304, https://doi.org/10.1016/j.jiec.2022.07.019, 297.
[33] B. Yan, X. Li, Z. Bai, Y. Zhao, L. Dong, X. Song, D. Li, C. Langford, X. Sun, Crumpled reduced graphene oxide conformally encapsulated hollow V_2O_5 nano/microsphere achieving brilliant lithium storage performance, Nano Energy 24 (2016) 32–44, https://doi.org/10.1016/j.nanoen.2016.04.002, 32.
[34] M. Songpanit, K. Boonyarattanakalin, W. Pecharapa, W. Mekprasart, ZnO nanostructures synthesized by one-step sol-gel process using different zinc precursors, J. Metals, Mater. Miner. 34 (3) (2024) 1968, https://doi.org/10.55713/jmmm.v34i3.1968.
[35] C. Sun, J. Pan, X. Fu, D. Ma, L. Cui, W. Yao, H. Hao, M. Li, A. Du, Q. Wang, Homogeneous encapsulation of Si/SnO_2 nanospheres in tunable carbon electrospinning nanofibers for high-performance lithium-ion battery, J. Energy Storage 88 (2024) 111576, https://doi.org/10.1016/j.est.2024.111576.
[36] A.M. Colclasure, K.A. Smith, R.J. Kee, Modeling detailed chemistry and transport for solid-electrolyte-interface (SEI) films in Li–ion batteries, Electrochim. Acta 58 (2011) 33–43, https://doi.org/10.1016/j.electacta.2011.08.067, 33.
[37] M. Gaberšček, Impedance spectroscopy of battery cells: theory versus experiment, Current Opinion Electrochem. 32 (2022) 100917, https://doi.org/10.1016/j.coelec.2021.100917.
[38] A.-M. Li, Z. Wang, T.P. Pollard, W. Zhang, S. Tan, T. Li, C. Jayawardana, S.-C. Liou, J. Rao, B.L. Lucht, E. Hu, X.-Q. Yang, O. Borodin, C. Wang, High voltage electrolytes for lithium-ion batteries with micro-sized silicon anodes, Nat. Commun. 15 (1) (2024) 1206, https://doi.org/10.1038/s41467-024-45374-0.
[39] N. Issatayev, K. Tassybay, N.-L. Wu, A. Nurpeissova, Z. Bakenov, G. Kalimuldina, LiF modified hard carbon from date seeds as an anode material for enhanced low-temperature lithium-ion batteries, Carbon N Y 229 (2024) 119479, https://doi.org/10.1016/j.carbon.2024.119479.
[40] D.D. Khumujam, T. Kshetri, T.I. Singh, N.H. Kim, J.H. Lee, Fibrous asymmetric supercapacitor based on wet spun MXene/PAN Fiber-derived multichannel porous MXene/CF negatrode and $NiCo_2S_4$ electrodeposited MXene/CF positrode, Chem. Eng. J. 449 (2022) 137732, https://doi.org/10.1016/j.cej.2022.137732.
[41] C. Chen, H. Xue, Q. Hu, M. Wang, P. Shang, Z. Liu, T. Peng, D. Zhang, Y. Luo, Construction of 3D porous $Cu_{1.81}S$/nitrogen-doped carbon frameworks for ultrafast and long-cycle life sodium-ion storage, Int. J. Miner., Metallurgy Mater. 32 (1) (2024) 191–200, https://doi.org/10.1007/s12613-024-2890-z, 191.
[42] C. Shi, Z. Long, C. Wu, H. Dai, Z. Li, H. Qiao, K. Liu, Q.H. Fan, K. Wang, Multi-pleated alkalized $Ti_3C_2T_x$ MXene-based sandwich-like structure composite nanofibers for high-performance sodium/lithium storage, Small 19 (48) (2023) 2303802, https://doi.org/10.1002/smll.202303802.
[43] N. Wu, Z. Zhao, R. Hua, X. Wang, Y. Zhang, J. Li, G. Liu, D. Guo, G. Sun, X. Liu, J. Zhang, Pre-doping of dual-functional sodium to weaken Fe-S bond and stabilize interfacial chemistry for high-rate reversible sodium storage, Adv. Energy Mater. 14 (30) (2024) 2400371, https://doi.org/10.1002/aenm.202400371.

Supporting Information

MXene carbon nanofiber-coated V_2O_3 hollow nanospheres as a Free-Standing flexible anode for lithium-ion batteries

Binhe Feng[a], Deyang Zhang*[a], Wenbo guo[a], Di Wang[a], Jinbing Cheng[b], Kangwen Qiu[c], Mengzhen Du[a], Jin Chang [ad], Paul K. Chu [e], Yongsong Luo *[ab]

[a] *Henan Joint International Research Laboratory of New Energy Storage Technology, Xinyang Normal University, Xinyang 464000, P. R. China.*

E-mail: zdy@xynu.edu.cn ， ysluo@xynu.edu.cn

[b] *College of Physics and Electronic Engineering, Nanyang Normal University, Nanyang 473061, P. R. China E-mail: chengjinbing1988@163.com*

[c] *College of Energy Engineering, Huanghuai University, Zhumadian, Henan 463000, China*

[d] *Pingdingshan University, Pingdingshan 467000, P. R. China*

[e]*Department of Physics, Department of Materials Science & Engineering, and Department of Biomedical Engineering, City University of Hong Kong, Tat Chee Avenue, Kowloon, Hong Kong, China*

Electrochemical evaluation

The electrochemical measurements were conducted using CR2032-type coin cells assembled in an argon-filled glove box with water and oxygen contents below 0.1 ppm. The as-synthesized V_2O_3@MXene/CNFs membrane was cut into free-standing electrodes with a diameter of 11 mm and a thickness of 0.1 mm (The mass of a single electrode is about 0.0030 g-0040 g, the area is 0.94985 cm^2). Because it is a self-supporting electrode, no metal current collector is required or any additives (e.g., conductive carbon or binder) was required. In the lithium ion batteries, Li metal was used as the counter and reference electrode and microporous Celgard 2400 membrane was used as the separator. The electrolyte was composed of a solution of 1 mol L-1 LiPF6 dissolved in a mixture of ethyl carbonate and dimethyl carbonate (1/1; v/v) with the addition of 5 wt% fluoroethylene carbonate.

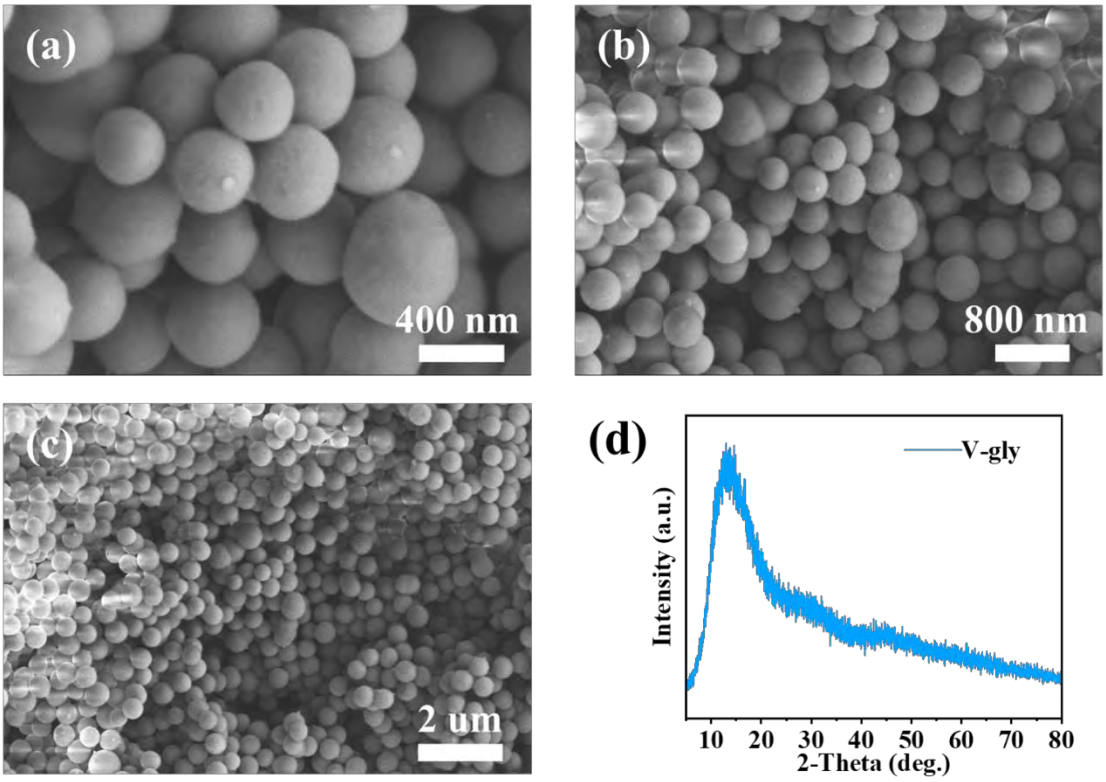

Figure S1. (a-c) SEM images of V-gly and (d) XRD patterns of V-gly.

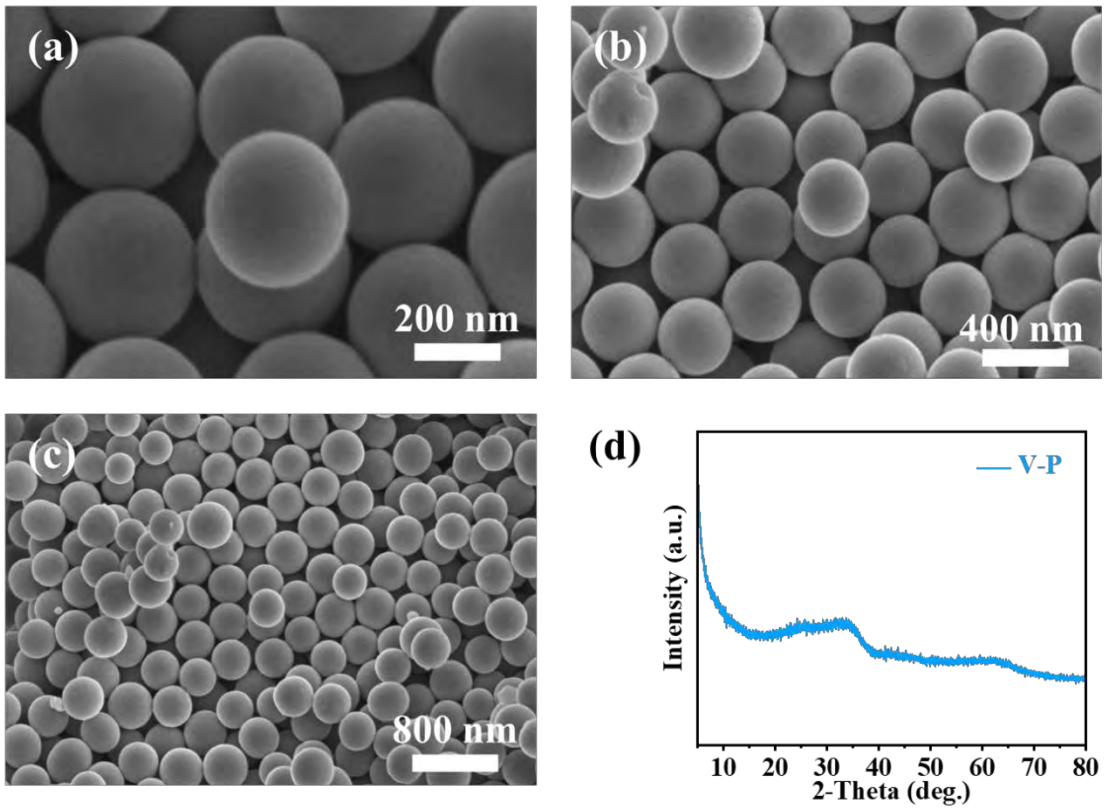

Figure S2. (a-c) SEM images of V-P and (d) XRD patterns of V-P.

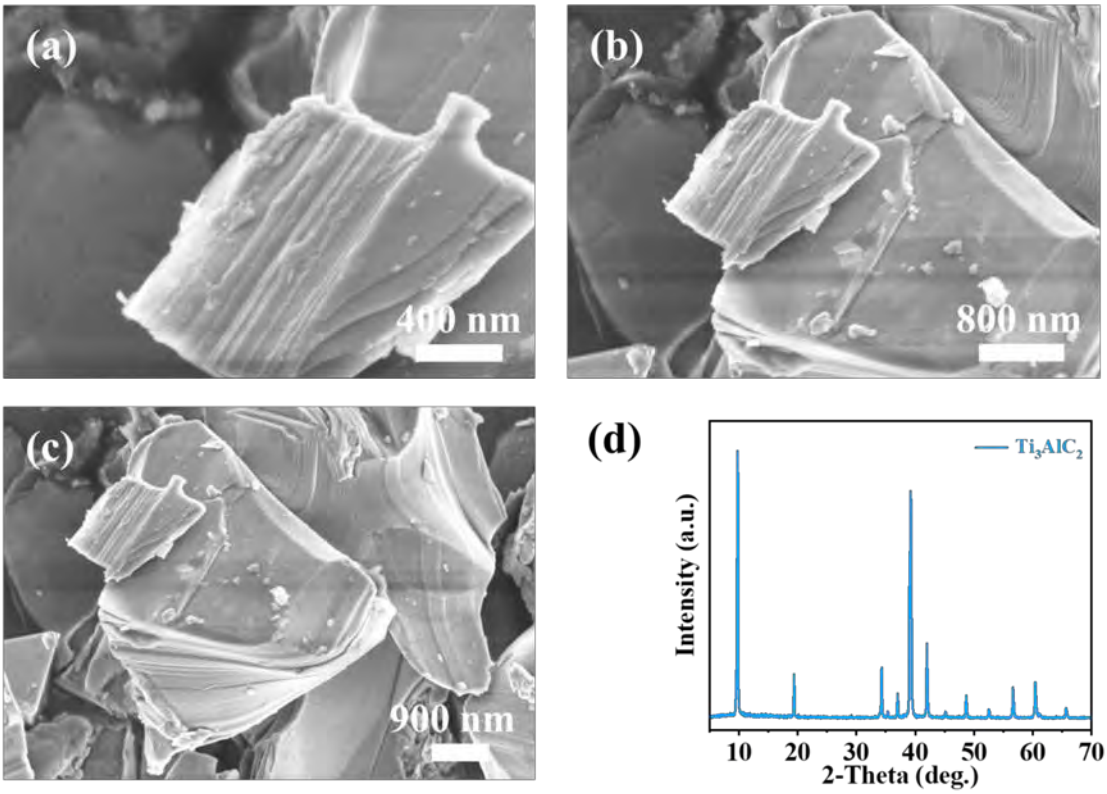

Figure S3. (a-c) SEM images of Ti_3AlC_2 and (d) XRD patterns of Ti_3AlC_2.

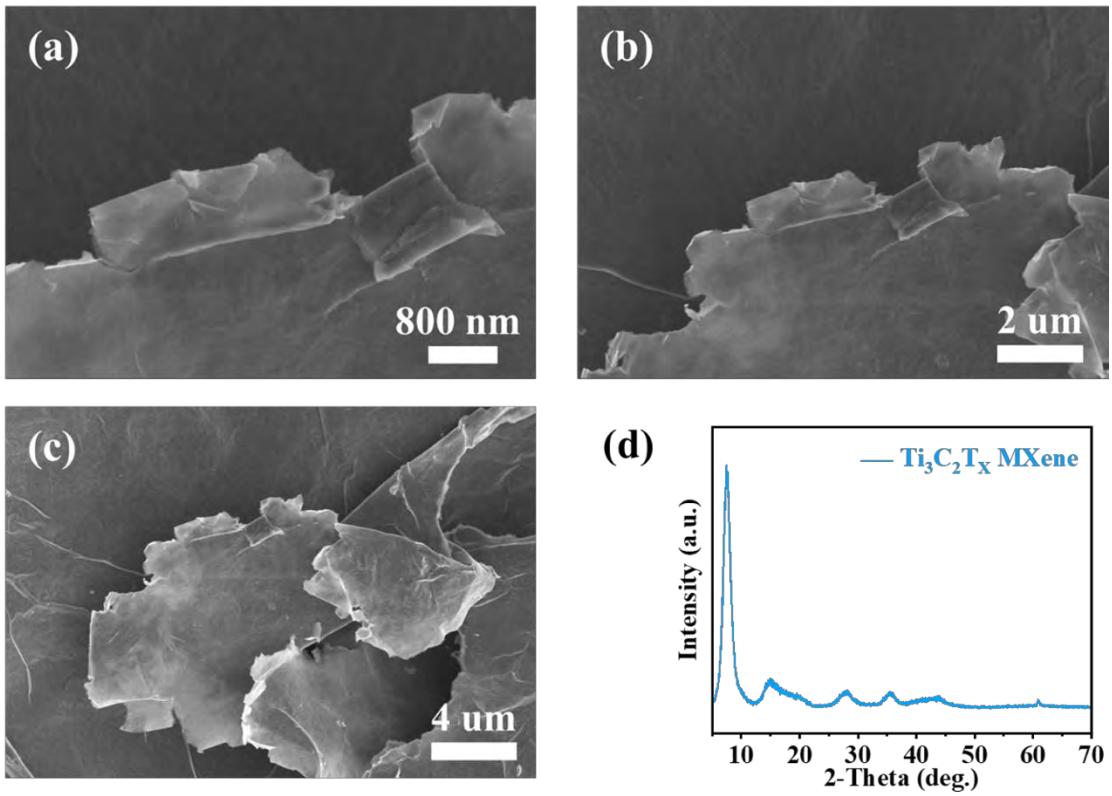

Figure S4. (a-c) SEM images of $Ti_3C_2T_X$ MXene and (d) XRD patterns of $Ti_3C_2T_X$ MXene.

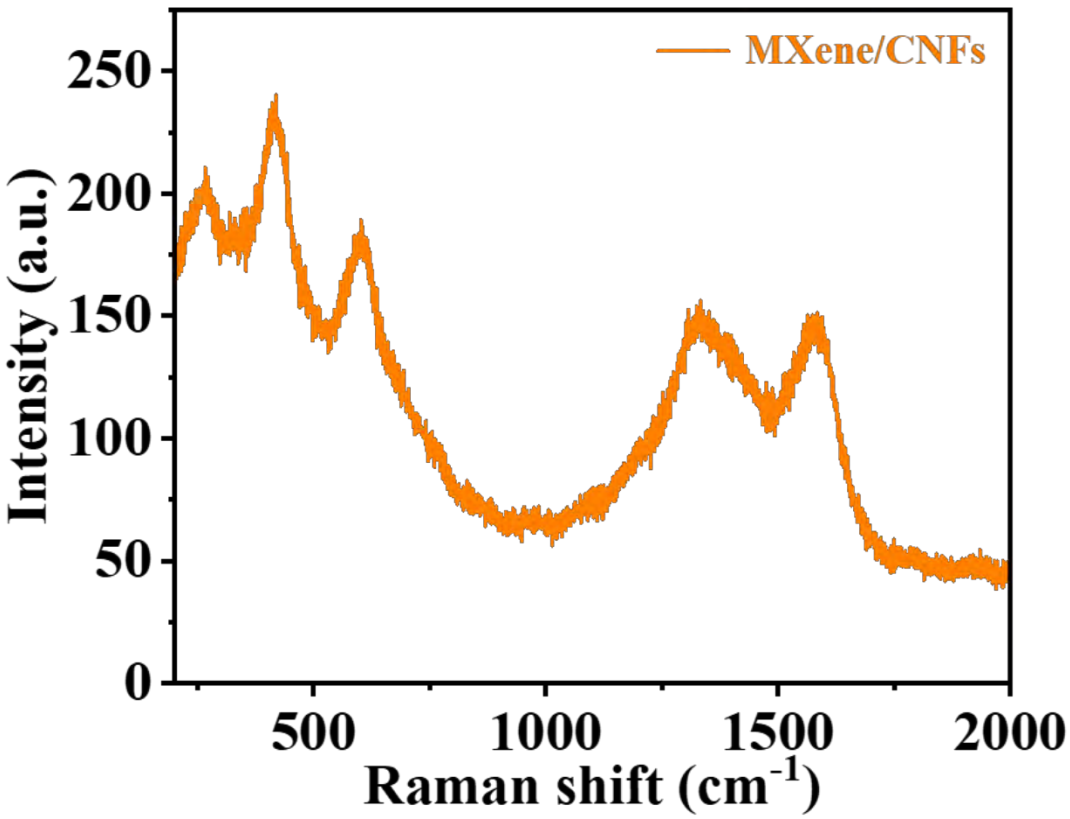

Figure S5. Raman scattering spectrum of MXene/CNFs.

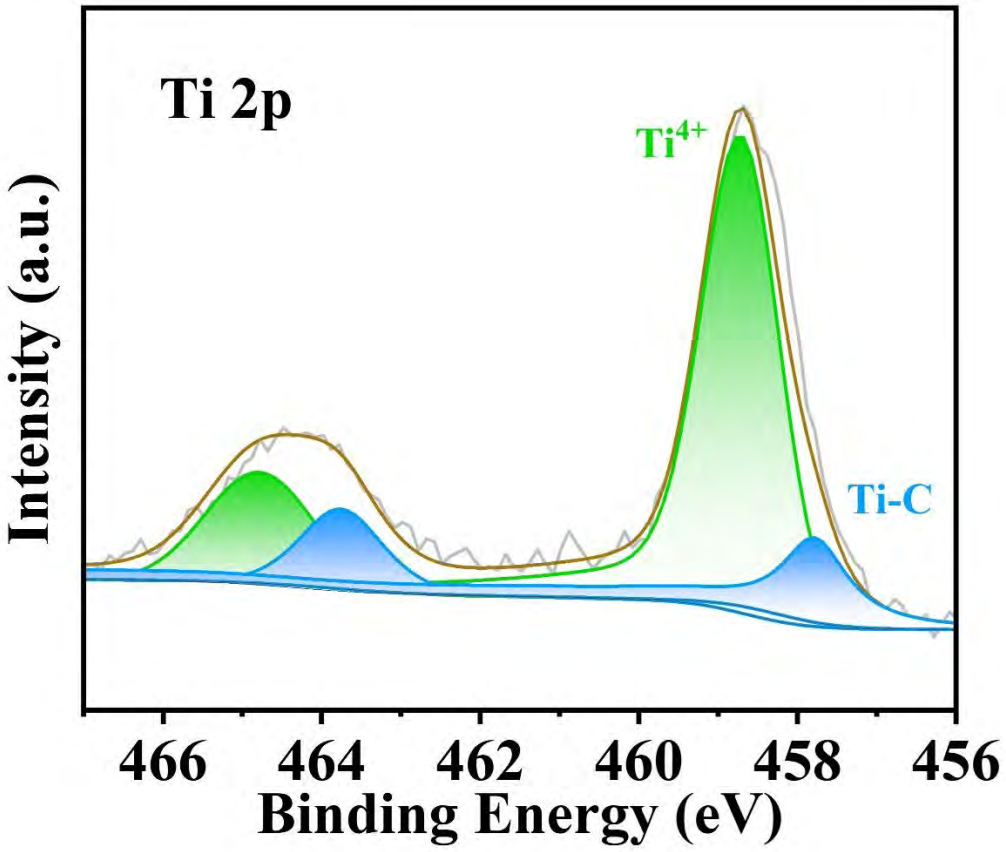

Figure S6. XPS Ti 2p spectrum.

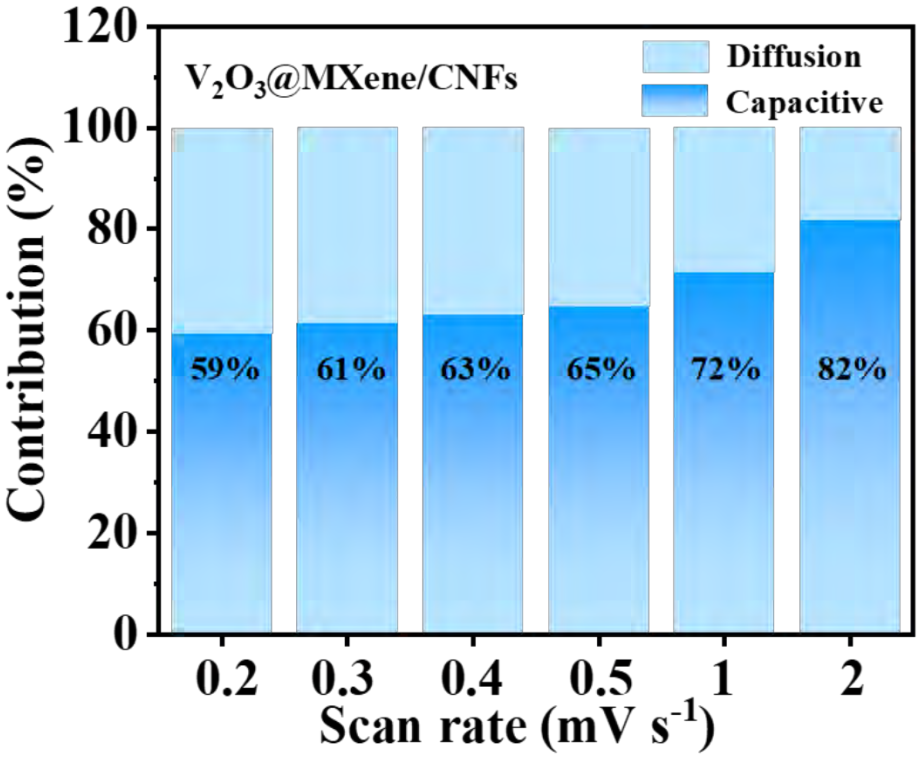

Figure S7. Percentages of diffusion-controlled and capacitance-controlled processes at various sweeping rates.

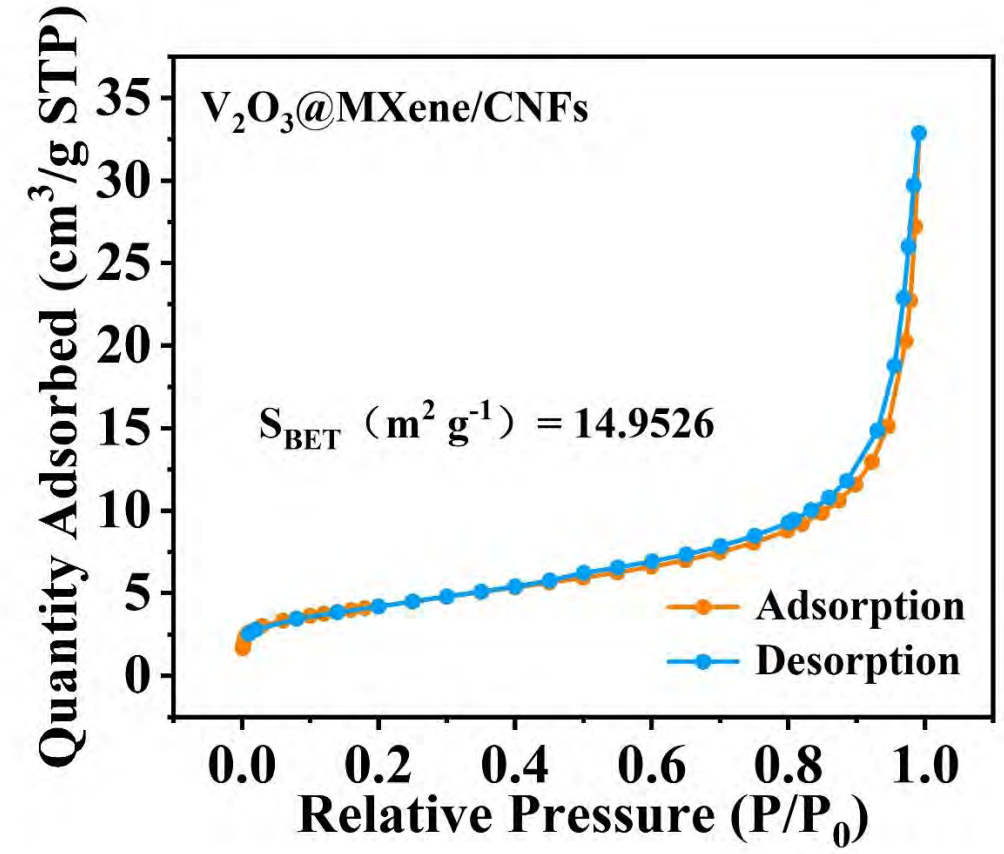

Figure S8. N_2 adsorption-desorption isotherm.

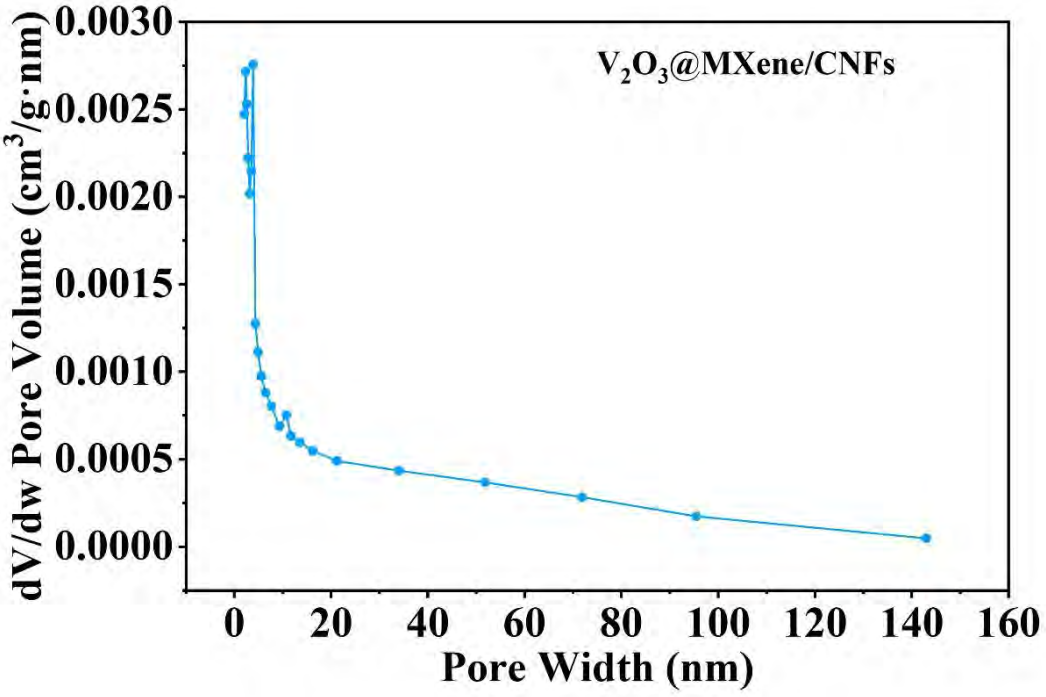

Figure S9. pore size distribution of V_2O_3@MXene/CNFs composite.

Samples	Capacity performance	Ref
V_2O_3@MXene/CNFs	651.88, 563.66, 485.67, 386.56, 300.62, 118.02 mAh g^{-1} at 0.1, 0.2, 0.5, 1, 2, 5 A g^{-1}	This work
V_2O_3/C/SS	613, 564, 515, 397, 310 mAh g^{-1} at 50, 100, 200, 500, 1000 mA g^{-1}	[1]
V_2O_5/TiO_2@Ti_3C_2-Mene	476.3, 403.4, 358.3, 315.2, 297.1, 259.3, 163.5 mAh g^{-1} at 0.1, 0.2, 0.4, 0.6, 0.8, 1.2 A g^{-1}	[2]
TiO_2-OV/MXene	369.8, 237.9, 215.2, 199.3, 182.6, 153.2, 123.3 mAh g^{-1} at 0.1, 0.2, 0.5, 1, 2, 5, 10 A g^{-1}	[3]
VBO_3/V_2O_3@C	927, 746, 629, 310 mAh g^{-1} at 15, 45, 75, 150, 450 mA g^{-1}	[4]
V_2O_3/C-M	337, 269, 183 mA g^{-1} at 100, 200, 500 mA g^{-1}	[5]

Table 1. Compare the electrochemical performance of vanadium oxide-based lithium battery electrodes studied in previous studies with that of this study.

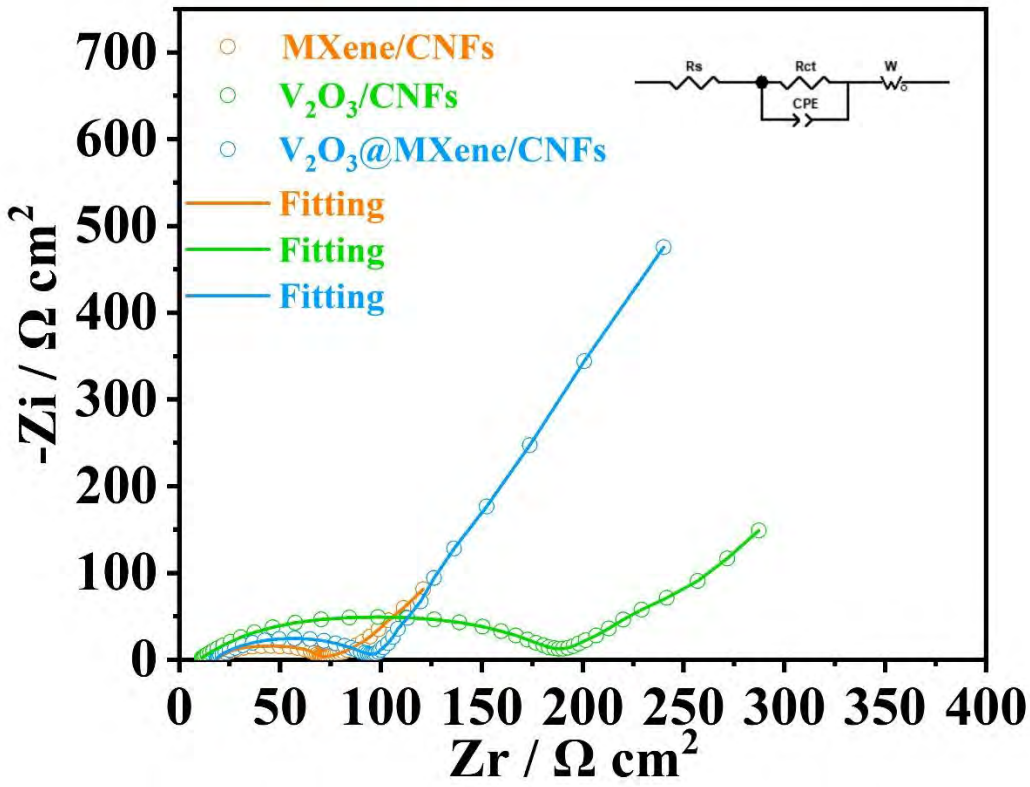

Figure S11. ELS data fitting lines and equivalent circuit diagrams.

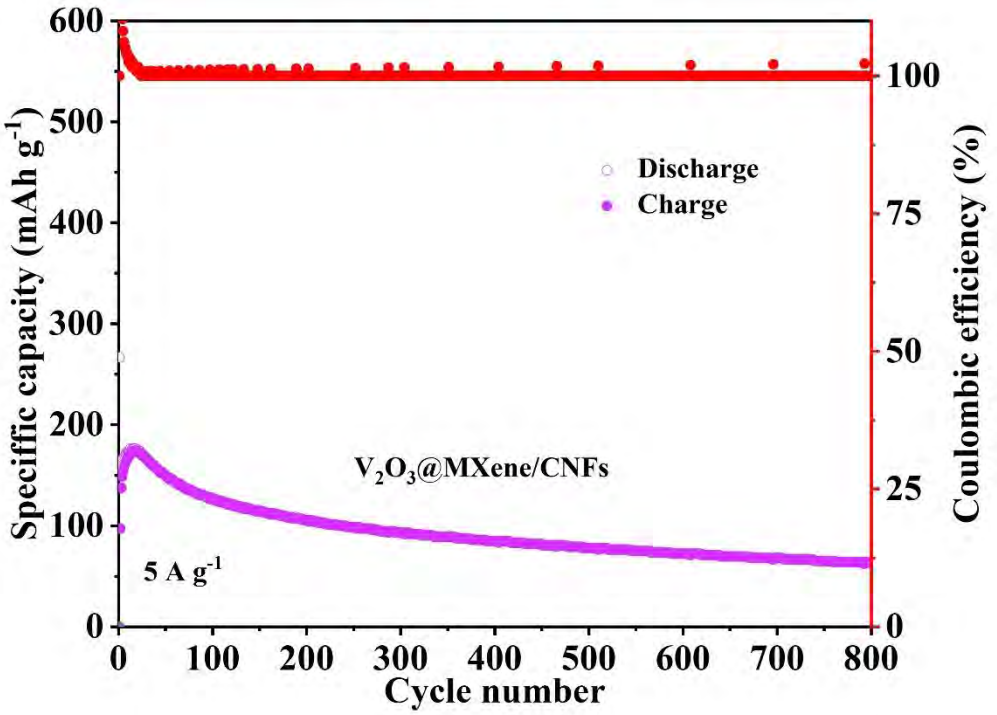

Figure S12. The cycling performance of pouch cell with V_2O_3@Mene/CNFs fibers as cathode and Li metal as anode at 180° bending angle a high density of 5 A g^{-1}.

Figure S13. The 180° bending photo.

samples	Conductivity range (S/cm)	Average electrical conductivity (S/cm)
V_2O_3@MXene/CNFs	0.001438 - 0.001548	0.001492
V_2O_3/CNFs	0.000478 - 0.001395	0.000899

Table 2. The conductivity range and average value of V_2O_3@MXene/CNFs and V_2O_3/CNFs tested by a four-probe tester.

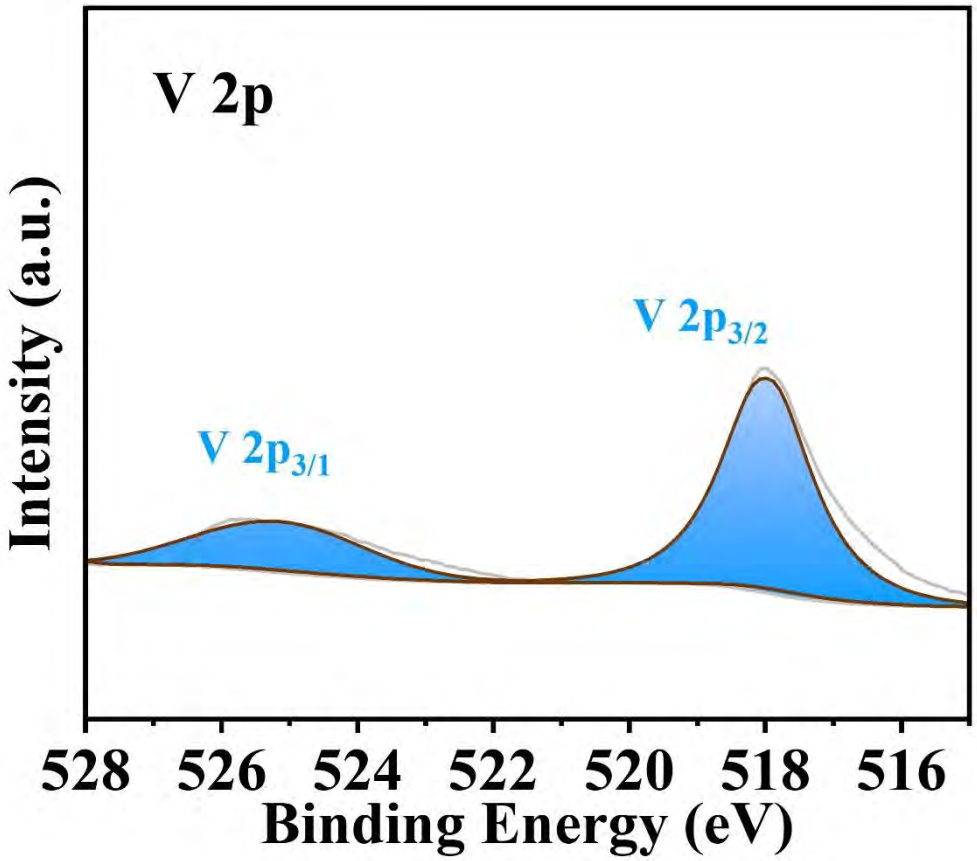

Figure S14. The XPS spectrum after the loop.

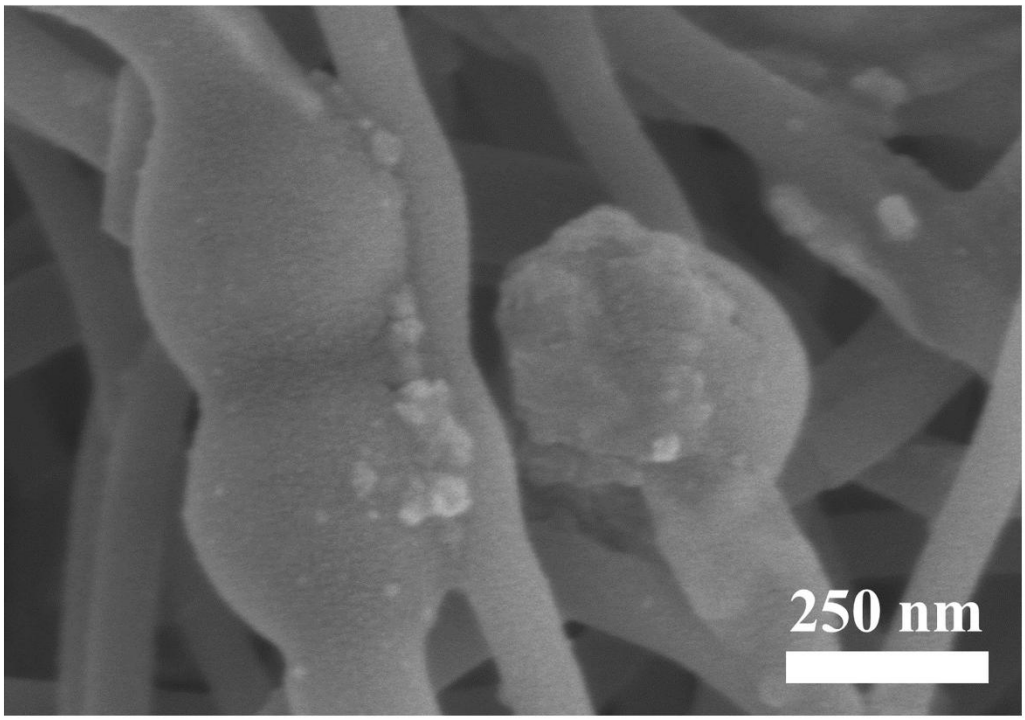

Figure S15. The SEM spectrum after the loop.

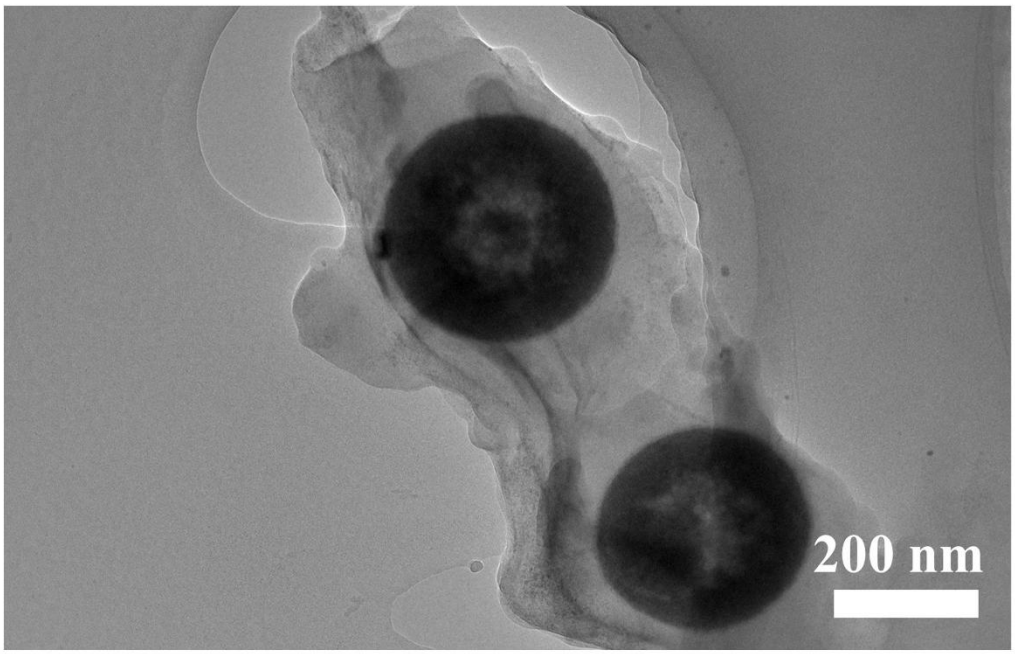

Figure S16. The TEM spectrum after the loop.

[1] Y. Tian, J. Zhang, T.A. Otitoju, H. Wang, H. Chen, L. Zhu, Z. Feng, T. Sun, Effective transportation of electrons/Li ions in V_2O_3 nanoparticle/carbon-coated stainless steel composite electrodes for lithium-ion storage, Journal of Industrial and Engineering Chemistry, 114 2022, 297 297-304, http://dx.doi.org/10.1016/j.jiec.2022.07.019.

[2] W. Myint, K. Lolupiman, C. Yang, P. Woottapanit, W. Limphirat, P. Kidkhunthod, M. Muzakir, M. Karnan, X. Zhang, J. Qin, Exploring the Electrochemical Superiority of V_2O_5/TiO_2@Ti_3C_2-MXene Hybrid Nanostructures for Enhanced Lithium-Ion Battery Performance, ACS Applied Materials & Interfaces, 16 2024 40, 53764 53764-53774, http://dx.doi.org/10.1021/acsami.4c10656.

[3] Z. Zhu, Y. Shen, Z. Pu, H. Liu, D. Liu, Y. Li, Convenient preparation of TiO_2-x/MXene composites and their performance as anodes for all-climate lithium-ion batteries, Journal of Power Sources, 630 2025, 236112, http://dx.doi.org/10.1016/j.jpowsour.2024.236112.

[4] S. Han, Y. Han, S. Liu, Y. Liu, X. Yang, K. Feng, VBO_3/V_2O_3@C heterogeneous anode material with high-specific-capacity and high-stability for lithium-ion batteries, Journal of Energy Storage, 101 2024, 113990, http://dx.doi.org/10.1016/j.est.2024.113990.

[5] G.S. Zakharova, E. Thauer, A.N. Enyashin, L.F. Deeg, Q. Zhu, R. Klingeler, V_2O_3/C composite fabricated by carboxylic acid-assisted sol–gel synthesis as anode material for lithium-ion batteries, Journal of Sol-Gel Science and Technology, 98 2021 3, 549 549-558, http://dx.doi.org/10.1007/s10971-021-05523-z.